

Strain Analysis by a Total Generalized Variation Regularized Optical Flow Model

Frank Balle*, Tilmann Beck*, Dietmar Eifler*, Jan Henrik Fitschen[†],
Sebastian Schuff*, and Gabriele Steidl[†]

April 21, 2017

Abstract

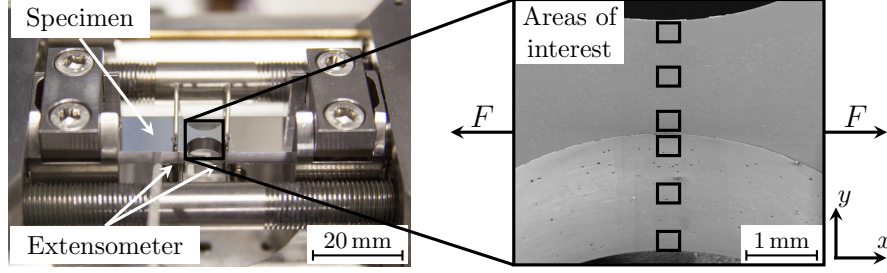
In this paper we deal with the important problem of estimating the local strain tensor from a sequence of micro-structural images realized during deformation tests of engineering materials. Since the strain tensor is defined via the Jacobian of the displacement field, we propose to compute the displacement field by a variational model which takes care of properties of the Jacobian of the displacement field. In particular we are interested in areas of high strain. The data term of our variational model relies on the brightness invariance property of the image sequence. As prior we choose the second order total generalized variation of the displacement field. This prior splits the Jacobian of the displacement field into a smooth and a non-smooth part. The latter reflects the material cracks. An additional constraint is incorporated to handle physical properties of the non-smooth part for tensile tests. We prove that the resulting convex model has a minimizer and show how a primal-dual method can be applied to find a minimizer. The corresponding algorithm has the advantage that the strain tensor is directly computed within the iteration process. Our algorithm is further equipped with a coarse-to-fine strategy to cope with larger displacements. Numerical examples with simulated and experimental data demonstrate the very good performance of our algorithm. In comparison to state-of-the-art engineering software for strain analysis our method can resolve local phenomena much better.

1 Introduction

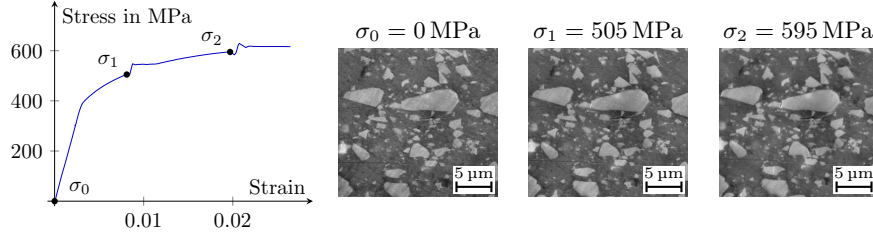
The (Cauchy) strain tensor plays a fundamental role in mechanical engineering for deriving local mechanical properties of materials. In this paper, we

*Department of Mechanical and Process Engineering, University of Kaiserslautern, Germany, {balle,beck,eifler,schuff}@mv.uni-kl.de.

[†]Department of Mathematics, University of Kaiserslautern, Germany, {fitschen,steidl}@mathematik.uni-kl.de.



(a) Experimental setup for the tensile test inside a scanning electron microscope. Left: Test material within the microscope. Right: Part of the material with the regions of interest, where a sequence of images (micrographs) is taken for increasing load.



(b) Stress-strain curve with three selected micrographs taken under increasing load. The stress $\sigma = \frac{F}{A_0}$ is defined as the applied force F divided by the initial cross section of the specimen A_0 . The (global) strain is defined as the relative elongation of the specimen measured by the extensometer.

Figure 1: Illustration of an in-situ tensile test.

are interested in estimating the strain tensor from a sequence of microstructural images of a certain material acquired during in-situ deformation tests. An experimental setup of a tensile test is shown in Figure 1.

Let $u := (u_1, u_2)^T$ be the displacement field that describes how each point moves from one image to another. For deformations of a continuum body, the strain tensor ε is defined via the Jacobian of the displacement field u by

$$\begin{aligned} \varepsilon &= \begin{pmatrix} \varepsilon_{11} & \varepsilon_{12} \\ \varepsilon_{12} & \varepsilon_{22} \end{pmatrix} := \frac{1}{2} (\nabla u + \nabla u^T) \\ &= \begin{pmatrix} \partial_x u_1 & \frac{1}{2}(\partial_y u_1 + \partial_x u_2) \\ \frac{1}{2}(\partial_y u_1 + \partial_x u_2) & \partial_y u_2 \end{pmatrix}. \end{aligned} \quad (1)$$

State-of-the-art software packages for strain analysis like Veddac [12], VIC [14], NCorr [5], and [24, 29, 32] apply correlation based methods to estimate the displacement field and use the result to compute the strain tensor. Roughly speaking, correlation based methods compare certain windows around each pixel in a predefined search window. Due to the extent of the window around the pixels and since the displacement is often only computed on a coarser grid to reduce the computational effort, the local resolution of

these methods is limited. This is especially a drawback when we are interested in the local strain behavior and the appearance of microstructural damage.

In this paper, we propose to use a variational model to compute the displacement field u from a sequence of images f . Variational models are composed of a data term $E_{\text{Data}}(u; f)$, which incorporates the information given by the image sequence, and a prior $E_{\text{Reg}}(u)$, which has to be chosen in such a way that its minimizer reflects known or desirable properties of the displacement field:

$$\arg \min_u E(u), \quad E(u) := E_{\text{Data}}(u; f) + \lambda E_{\text{Reg}}(u).$$

In image processing, the apparent displacement u between image frames is known as optical flow. Variational methods for optical flow estimation go back to Horn and Schunck [19], and there is a vast number of refinements and extensions of their approach. We refer to [4] for a comprehensive overview. In particular, optical flow models with priors containing higher order derivatives of the flow were successfully used, e.g. in [1, 6, 13, 18, 22, 30, 31, 33, 34].

Although it seems natural to apply ideas from variational optical flow models also for strain analysis, such methods have rarely been addressed in the literature. The papers [1, 13] aim at computing derivatives simultaneously to the optical flow field but are not related to engineering applications. The computation of the (Lagrangian) strain tensor by a variational method was addressed in [17]. There, the authors proposed a *smooth* fourth order optical flow model which directly computes the strain tensor from an image sequence obtained in a biaxial tensile test with an elastomer. In contrast to our work, they were interested in the macro-scale behavior and compute the minimizer of their smooth energy function by solving the corresponding Euler-Lagrange equations.

We propose a data term $E_{\text{Data}}(u; f)$ based on the brightness invariance assumption of the image sequence, which is usual in optical flow estimation. The more interesting part is the choice of the prior, where we have in mind that we are interested in local variations of the Jacobian of the displacement field, i.e. of the strain. In the conference paper [3], we built up on the assumption that the displacement field u is additively composed of a non-smooth part v and a smooth part w . Then, we penalized the Jacobian of v and the second order derivative of w by an infimal convolution prior. The infimal convolution (IC) of first and second order derivatives was introduced in imaging by Chambolle and Lions [10]. For a recent generalization called ICTV, we refer to [18]. In this paper, we will see that it is better for our task to split the Jacobian of u instead of u itself. To this end, we apply the second order total generalized variation (TGV) of the displacement field as prior. For tensile tests, a physical prior on the non-smooth part of the strain is added. The TGV of functions was introduced by Bredies, Kunisch,

and Pock [7] for image restoration tasks and has meanwhile found many applications. For a discrete variant, see also [25, 26]. In particular, TGV regularization was successfully used in connection with optical flow in [6, 22, 31]. Our applications show the potential of the method in an impressive way.

The resulting variational model is convex and a minimizer can be computed with primal-dual methods, which are meanwhile standard in image processing. The corresponding algorithm computes the strain tensor directly within the iteration process. This is an advantage compared to standard engineering software, which estimates the displacement field by correlation based methods first and then computes its Jacobian. Our algorithm is further equipped with a coarse-to-fine strategy to cope with larger displacements as proposed, e.g., in [2, 8, 27, 28].

We demonstrate by artificial and real-world examples that the proposed model leads to very good results, which cannot be obtained by state-of-the-art software packages. With our extensive numerical results, we aim at convincing engineers of the advantages of the proposed method.

2 Model

We start with the continuous model and turn to the discrete model for digital images afterwards. The reason is that the discrete notation appears more clumsy and it is easier to get the clue from the continuous notation.

Continuous model. Suppose that we are given gray-valued images

$$f_1, f_2: \mathbb{R}^2 \supset \Omega \rightarrow \mathbb{R}.$$

We are interested in the flow field $u = (u_1, u_2): \Omega \rightarrow \mathbb{R}^2$, which describes how f_1 transforms into f_2 . Here, we focus on the brightness invariance assumption, which reads with $\mathbf{x} := (x, y)$ as

$$f_1(\mathbf{x}) - f_2(\mathbf{x} + u(\mathbf{x})) = f_1(\mathbf{x}) - f_2(x + u_1(\mathbf{x}), y + u_2(\mathbf{x})) \approx 0. \quad (2)$$

A first order Taylor expansion around an initial optical flow field $\bar{u} = (\bar{u}_1, \bar{u}_2)$ gives

$$f_2(\mathbf{x} + u(\mathbf{x})) \approx f_2(\mathbf{x} + \bar{u}(\mathbf{x})) + \left\langle \begin{pmatrix} \partial_x f_2 \\ \partial_y f_2 \end{pmatrix} (\mathbf{x} + \bar{u}(\mathbf{x})), u(\mathbf{x}) - \bar{u}(\mathbf{x}) \right\rangle. \quad (3)$$

Plugging (3) into (2), we obtain

$$0 \approx f_1(\mathbf{x}) - f_2(\mathbf{x} + \bar{u}(\mathbf{x})) - \left\langle \begin{pmatrix} \partial_x f_2 \\ \partial_y f_2 \end{pmatrix} (\mathbf{x} + \bar{u}(\mathbf{x})), u(\mathbf{x}) - \bar{u}(\mathbf{x}) \right\rangle.$$

Later, we apply a coarse-to-fine scheme [2, 8] and use the result from one scale as an initialization for the next one. Applying a non-negative increasing function $\varphi: \mathbb{R} \rightarrow \mathbb{R}_{\geq 0}$ results in the data term

$$\int_{\Omega} \varphi \left(- \left\langle \begin{pmatrix} \partial_x f_2(\mathbf{x} + \bar{u}(\mathbf{x})) \\ \partial_y f_2(\mathbf{x} + \bar{u}(\mathbf{x})) \end{pmatrix}, u(\mathbf{x}) - \bar{u}(\mathbf{x}) \right\rangle - f_2(\mathbf{x} + \bar{u}(\mathbf{x})) + f_1(\mathbf{x}) \right) d\mathbf{x}. \quad (4)$$

For the task at hand, we need a prior which recognizes local changes in the displacement field. Therefore, it seems to be useful to consider the smooth global and non-smooth local behavior of the displacement field.

In [3], we assumed that $u = v + w$ can be decomposed additively into a non-smooth part $v \in W^{1,1}(\Omega, \mathbb{R}^2)$ and a smooth part w with $\nabla w \in W^{1,1}(\Omega, \mathbb{R}^d)$. Here, $W^{1,1}(\Omega, \mathbb{R}^d)$ denotes the Sobolev space of functions mapping from Ω into \mathbb{R}^d with absolutely integrable weak first order partial derivatives. The smoothness of w is enforced by penalizing the Frobenius norm of its Hessian $\|\nabla^2 w\|_F$. The non-smooth part v is penalized by the Frobenius norm of its Jacobian $\|\nabla v\|_F$, which can be seen as total variation regularization of v [23]. The total variation favors piecewise constant functions with small boundaries. Then, we suggested the prior

$$\begin{aligned} \text{IC}(u) &:= \inf_{v+w=u} \left\{ \int_{\Omega} \lambda_1 \|\nabla v\|_F + \lambda_2 \|\nabla^2 w\|_F d\mathbf{x} \right\} \\ &= \inf_w \left\{ \int_{\Omega} \lambda_1 \|\nabla u - \nabla w\|_F + \lambda_2 \|\nabla^2 w\|_F d\mathbf{x} \right\}, \end{aligned} \quad (5)$$

which is the IC of $\|\nabla \cdot\|_F$ and $\|\nabla^2 \cdot\|_F$.

In this paper, we decompose $\nabla u = a + \tilde{a}$ instead of u , where we suppose that $\tilde{a} \in L_1(\Omega, \mathbb{R}^4)$ and $a \in W^{1,1}(\Omega, \mathbb{R}^4)$. We use the second order TGV of the displacement field u as a prior, which reads in a simplified version as

$$\begin{aligned} \text{TGV}(u) &:= \inf_{a+\tilde{a}=\nabla u} \left\{ \int_{\Omega} \lambda_1 \|\tilde{a}\|_F + \lambda_2 \|\nabla a\|_F d\mathbf{x} \right\} \\ &= \inf_a \left\{ \int_{\Omega} \lambda_1 \|\nabla u - a\|_F + \lambda_2 \|\nabla a\|_F d\mathbf{x} \right\}. \end{aligned} \quad (6)$$

Of course, if a is conservative, i.e., the Jacobian of some function w , then IC and TGV coincide. However, the latter is in general not the case. In our applications, cracks are reflected by the non-smooth part \tilde{a} of ∇u . Here, it is important to notice the following difference: the IC prior (5) enforces sparsity of the Jacobian ∇v of the non-smooth part v of u ; while the TGV prior enforces sparsity of the non-smooth part \tilde{a} of the Jacobian ∇u of u .

Discrete model. In practice, we are concerned with images $f_1, f_2: \mathcal{G} \rightarrow \mathbb{R}$ defined on a two-dimensional rectangular grid $\mathcal{G} := \{1, \dots, N_1\} \times \{1, \dots, N_2\}$.

Besides this notion, we use the alternative representation of an image f as a vector of length $N = |\mathcal{G}| = N_1 N_2$. In the task at hand, we are given micrographs f_1 and f_2 , e.g. from a tensile test, corresponding to different loads as depicted in Figure 1. Considering only grid points $\mathbf{x} = \mathbf{j} \in \mathcal{G}$ and assuming for a moment that also the partial derivatives of f_2 are given, the data term in (4) becomes

$$\sum_{\mathbf{j} \in \mathcal{G}} \varphi \left(- \left\langle \begin{pmatrix} \partial_x f_2(\mathbf{j} + \bar{u}(\mathbf{j})) \\ \partial_y f_2(\mathbf{j} + \bar{u}(\mathbf{j})) \end{pmatrix}, u(\mathbf{j}) - \bar{u}(\mathbf{j}) \right\rangle - f_2(\mathbf{j} + \bar{u}(\mathbf{j})) + f_1(\mathbf{j}) \right). \quad (7)$$

This term is only well defined if $\mathbf{j} + \bar{u}(\mathbf{j}) \in \mathcal{G}$. Here, we use bilinear interpolation to compute the required values of f_2 between grid points: for given $f: \mathcal{G} \rightarrow \mathbb{R}$ assume that the four surrounding integer coordinates of $\mathbf{j} + \bar{u}(\mathbf{j})$ are (x_i, y_j) , $i, j = 1, 2$, where $x_1 = \lfloor x \rfloor$, $x_2 = x_1 + 1$, $y_1 = \lfloor y \rfloor$ and $y_2 = y_1 + 1$. These points can lie outside the grid. We assume mirror extension of the image at the boundary. Setting

$$\mathbf{j}_{ij} := (\min\{\max\{x_i, 1\}, N_1\}, \min\{\max\{y_j, 1\}, N_2\}), \quad i, j = 1, 2,$$

we approximate $f(\mathbf{j} + \bar{u}(\mathbf{j}))$ by

$$f(\mathbf{j} + \bar{u}(\mathbf{j})) \approx T_{\bar{u}} f(\mathbf{j}) := \begin{pmatrix} x_2 - x & x - x_1 \end{pmatrix} \begin{pmatrix} f(\mathbf{j}_{11}) & f(\mathbf{j}_{12}) \\ f(\mathbf{j}_{21}) & f(\mathbf{j}_{22}) \end{pmatrix} \begin{pmatrix} y_2 - y \\ y - y_1 \end{pmatrix}.$$

By $\nabla_x f$ we denote the forward differences in x -direction with Neumann boundary conditions defined as

$$(\nabla_x f)(\mathbf{j}) := \begin{cases} f(\mathbf{j} + (1, 0)) - f(\mathbf{j}) & \text{if } \mathbf{j} + (1, 0) \in \mathcal{G}, \\ 0 & \text{otherwise,} \end{cases} \quad \mathbf{j} \in \mathcal{G}.$$

Again, we use the notation $\nabla_x f$ both for the function and the vectorized version. Furthermore, we denote also the corresponding difference matrix by ∇_x . The differences in y -direction can be defined analogously. We replace the partial derivatives of f_2 in (7) by the forward differences $\nabla_x f_2, \nabla_y f_2$ and apply $T_{\bar{u}}$ to these differences which results in the data term

$$\sum_{\mathbf{j} \in \mathcal{G}} \varphi \left(- \left\langle \begin{pmatrix} T_{\bar{u}}(\nabla_x f_2)(\mathbf{j}) \\ T_{\bar{u}}(\nabla_y f_2)(\mathbf{j}) \end{pmatrix}, u(\mathbf{j}) - \bar{u}(\mathbf{j}) \right\rangle - T_{\bar{u}} f_2(\mathbf{j}) + f_1(\mathbf{j}) \right).$$

For our task, we use the function

$$\varphi(t) := |t|$$

because it is well-known that the ℓ_1 -norm reduces the influence of outliers. Then the data term can be rewritten in the convenient matrix-vector notation

$$E_{\text{Data}}(u; f_1, f_2) := \|(A \ B)u + c\|_1 = \|Au_1 + Bu_2 + c\|_1, \quad (8)$$

where

$$\begin{aligned} A &:= \text{diag} \left(T_{\bar{u}}(\nabla_x f_2) \right), \quad B := \text{diag} \left(T_{\bar{u}}(\nabla_y f_2) \right), \\ c &:= -\text{diag} \left(T_{\bar{u}}(\nabla_x f_2) \right) \bar{u}_1 - \text{diag} \left(T_{\bar{u}}(\nabla_y f_2) \right) \bar{u}_2 + T_{\bar{u}} f_2 - f_1. \end{aligned}$$

For the discrete versions of the TGV prior, we also need the backward differences $\tilde{\nabla}_x u$ in x -direction, i.e.,

$$(\tilde{\nabla}_x u)(\mathbf{j}) = \begin{cases} u(\mathbf{j}) - u(\mathbf{j} - (1, 0)) & \text{if } \mathbf{j} \pm (1, 0) \in \mathcal{G}, \\ 0 & \text{otherwise,} \end{cases} \quad \mathbf{j} \in \mathcal{G}$$

and analogously for the y -direction. We set

$$\nabla := \begin{pmatrix} \nabla_x \\ \nabla_y \end{pmatrix}, \quad \tilde{\nabla} := \begin{pmatrix} \tilde{\nabla}_x & \\ \frac{1}{2} \tilde{\nabla}_y & \frac{1}{2} \tilde{\nabla}_x \\ & \tilde{\nabla}_y \end{pmatrix},$$

and use the tensor products

$$\nabla u := (I_2 \otimes \nabla)u, \quad \tilde{\nabla} u := (I_2 \otimes \tilde{\nabla})u.$$

Denoting by $\|\cdot\|_{2,1}$ the mixed norm defined for $x \in \mathbb{R}^{dN}$ as

$$\|x\|_{2,1} := \sum_{i=1}^N \|(x_{i+jN})_{j=0}^{d-1}\|_2,$$

the discrete counterpart of the TGV prior in (6) reads

$$\text{TGV}(u) := \min_a \left\{ \lambda_1 (\|\nabla u - a\|_{2,1} + \lambda_2 \|\tilde{\nabla} a\|_{2,1}) \right\}. \quad (\text{TGV})$$

In summary, our model is given by

$$E_{\text{TGV}}(u) = \|(A \ B)u + c\|_1 + \min_a \left\{ \lambda_1 \|\nabla u - a\|_{2,1} + \lambda_2 \|\tilde{\nabla} a\|_{2,1} \right\}. \quad (9)$$

From a physical point of view, it makes sense to incorporate additional constraints on the displacement field or the strain. In the TGV model, we split the strain into parts representing the global and local features. With this interpretation, it is a reasonable assumption that for tensile tests the strain corresponding to local phenomena is positive in the direction of the applied force. This is motivated by the fact that cracks can only open or widen during a tensile test. Mathematically, if a force is applied in x -direction, we make the restriction $\nabla_x u_1 - a_1 \geq 0$, so that the model becomes

$$\begin{aligned} \tilde{E}_{\text{TGV}}(u) = & \|(A \ B)u + c\|_1 + \min_a \left\{ \lambda_1 \|\nabla u - a\|_{2,1} + \lambda_2 \|\tilde{\nabla} a\|_{2,1} \right\} \quad (10) \\ \text{subject to } & \nabla_x u_1 - a_1 \geq 0. \end{aligned}$$

Remark 1. *Let us emphasize that strain in materials science is only defined for continuous deformation. In this sense, it is not defined for cracks. In accordance with the definition (1) in the continuous setting, we refer to its discrete counterpart ∇u as the strain. Nevertheless, we will see later that strain in the classical sense is sometimes better resembled by the smooth part a .*

By the next proposition, the functions (9), resp. (10) possess minimizers under a mild assumption which was in particular fulfilled for all our practical examples.

Proposition 2. *Let $\ker((A \ B)) \cap \ker(\tilde{\nabla} \nabla) = \{0\}$. Then there exist minimizers of (9) and (10).*

Proof. It is sufficient to show that the continuous, convex function E in (9) is coercive, which implies the assertion for (9). Regarding (10), the assertion follows immediately since the function remains coercive after adding the constraint.

Assume in contrast that there exists a sequence $(u^{(r)})_{r \in \mathbb{N}}$ with $\|u^{(r)}\|_2 \rightarrow \infty$ but $E(u^{(r)}) \not\rightarrow \infty$ as $r \rightarrow \infty$. Then there exists a subsequence $(u^{(r_j)})_{j \in \mathbb{N}}$ such that $E(u^{(r_j)}) \leq C$ for all $j \in \mathbb{N}$ and some $C \in \mathbb{R}$. We split $u^{(r_j)} = u_a^{(r_j)} + u_b^{(r_j)}$ with $u_a^{(r_j)} \in \ker(\tilde{\nabla} \nabla)$ and $u_b^{(r_j)} \in \ker(\tilde{\nabla} \nabla)^\perp$, where $\ker(\tilde{\nabla} \nabla)^\perp$ denotes the orthogonal complement of $\ker(\tilde{\nabla} \nabla)$.

Suppose that $\|u_b^{(r_j)}\|_2 \rightarrow \infty$ as $j \rightarrow \infty$. We have

$$\begin{aligned} \text{TGV}(u^{(r_j)}) &= \min_a \left\{ \lambda_1 (\|\nabla u^{(r_j)} - a\|_{2,1} + \lambda_2 \|\tilde{\nabla} a\|_{2,1}) \right\} \\ &= \min_z \left\{ \lambda_1 (\|\nabla u_b^{(r_j)} - z\|_{2,1} + \lambda_2 \|\tilde{\nabla} z + \tilde{\nabla} \nabla u_a^{(r_j)}\|_{2,1}) \right\} \\ &= \min_z \left\{ \lambda_1 (\|\nabla u_b^{(r_j)} - z\|_{2,1} + \lambda_2 \|\tilde{\nabla} z\|_{2,1}) \right\}, \end{aligned}$$

where $z := a - \nabla u_a^{(r_j)}$. Using $\nabla u_b^{(r_j)} \in \ker(\tilde{\nabla})^\perp$ yields

$$\text{TGV}(u^{(r_j)}) \rightarrow \infty \quad \text{as } j \rightarrow \infty,$$

in contradiction to $E(u^{(r_j)}) \leq C$.

Assume that $\|u_b^{(r_j)}\|_2 \not\rightarrow \infty$ as $j \rightarrow \infty$. Then there exists a subsequence $(u_b^{(r_{j_l})})_{l \in \mathbb{N}}$ with $\|u_b^{(r_{j_l})}\|_2 \leq \tilde{C}$ for some $\tilde{C} \in \mathbb{R}$ and it follows

$$\begin{aligned} \|(A \ B)u^{(r_{j_l})} + c\|_1 &\geq \|(A \ B)u_a^{(r_{j_l})} + c\|_1 - \|(A \ B)u_b^{(r_{j_l})}\|_1 \\ &\geq \|(A \ B)u_a^{(r_{j_l})} + c\|_1 - \tilde{C}. \end{aligned}$$

Since $u_a^{(r_{j_l})} \notin \ker((A \ B))$, the right-hand side goes to $+\infty$ as $l \rightarrow \infty$, which is a contradiction. \square

3 Algorithm

In this section, we use the primal-dual hybrid gradient method with modified dual variable (PDHGMp) [11, 21] to compute a minimizer of (9). The minimization of (10) follows similarly.

We rewrite the minimization problem as

$$\begin{aligned} \min_{u,a,s,t} \{ & \|(A \ B)u + c\|_1 + \lambda_1 \|s\|_{2,1} + \lambda_2 \|t\|_{2,1} \} \\ \text{such that} \quad & \begin{pmatrix} \nabla & -I_{4N} \\ 0 & \widetilde{\nabla} \end{pmatrix} \begin{pmatrix} u \\ a \end{pmatrix} = \begin{pmatrix} s \\ t \end{pmatrix}. \end{aligned} \quad (11)$$

The basic PDHGMp algorithm for this problem is given in Algorithm 1. For the special form, we refer to [9, Alg. 8].

Algorithm 1 PDHGMp for optical flow and strain computation by E_{TGV} .

Initialization: $u^{(0)} = u_0$, $a^{(0)} = a_0$, $b_1^{(0)} = 0$, $b_2^{(0)} = \mathbf{0}$, $\bar{b}_1^{(0)} = \mathbf{0}$, $\bar{b}_2^{(0)} = \mathbf{0}$, $\theta = 1$, $\tau_1 = \frac{1}{4}$, $\tau_2 = \frac{1}{4}$.

for $r = 0, 1, \dots$ **do**

$$\begin{aligned} u^{(r+1)} &= \arg \min_{u \in \mathbb{R}^{2N}} \left\{ \|(A \ B)u + c\|_1 + \frac{1}{2\tau_1} \|u - (u^{(r)} - \tau_1 \tau_2 \nabla^T \bar{b}_1^{(r)})\|_2^2 \right\} \\ a^{(r+1)} &= a^{(r)} - \tau_1 \tau_2 (\widetilde{\nabla}^T \bar{b}_2^{(r)} - \bar{b}_1^{(r)}) \\ s^{(r+1)} &= \arg \min_{s \in \mathbb{R}^{4N}} \left\{ \lambda_1 \|s\|_{2,1} + \frac{\tau_2}{2} \|s - (b_1^{(r)} + \nabla u^{(r+1)} - a^{(r+1)})\|_2^2 \right\} \\ t^{(r+1)} &= \arg \min_{t \in \mathbb{R}^{6N}} \left\{ \lambda_2 \|t\|_{2,1} + \frac{\tau_2}{2} \|t - (b_2^{(r)} + \widetilde{\nabla} a^{(r+1)})\|_2^2 \right\} \\ b_1^{(r+1)} &= b_1^{(r)} + \nabla u^{(r+1)} - a^{(r+1)} - s^{(r+1)} \\ b_2^{(r+1)} &= b_2^{(r)} + \widetilde{\nabla} a^{(r+1)} - t^{(r+1)} \\ \bar{b}_1^{(r+1)} &= b_1^{(r+1)} + \theta(b_1^{(r+1)} - b_1^{(r)}) \\ \bar{b}_2^{(r+1)} &= b_2^{(r+1)} + \theta(b_2^{(r+1)} - b_2^{(r)}) \end{aligned}$$

Output: Strain components s and a , optical flow u

We have to comment on the proximal steps within the algorithm. The update for a is straightforward. Regarding s, t , observe that the problems can be separated into N subproblems, e.g. for s they have the form

$$\hat{s} = \arg \min_{s \in \mathbb{R}^4} \left\{ \|s\|_2 + \frac{\tau_2}{2\lambda_1} \|s - x\|_2^2 \right\},$$

where $x = (b_1^{(r)} + \nabla u^{(r+1)} - a^{(r+1)})_{i+jN, j=0, \dots, 3} \in \mathbb{R}^4$, $i \in 1, \dots, N$. The solution of these problems is given by a grouped or coupled shrinkage, see the appendix. If we extend the model by the positivity constraint, i.e. (10), the update step for s becomes a bit more involved since we need to compute N problems of the form

$$\hat{s} = \arg \min_{s \in \mathbb{R}^4} \left\{ \|s\|_2 + \iota_{\geq 0}(s_1) + \frac{\tau_2}{2\lambda_1} \|s - x\|_2^2 \right\}$$

with x as above. For $x_1 \geq 0$, the term $\iota_{\geq 0}(s_1)$ can be neglected and we end up with the usual coupled shrinkage. For $x_1 < 0$, we have $\hat{s}_1 = 0$ and for the remaining three components the usual coupled shrinkage can be applied.

Due to the diagonal structure of A and B , the proximal step to get u can be separated into N subproblems of the form

$$\hat{y} = \arg \min_{y \in \mathbb{R}^2} \left\{ |\alpha y_1 + \beta y_2 + \gamma| + \frac{1}{2} \|y - x\|_2^2 \right\}, \quad (12)$$

where $\alpha, \beta, \gamma \in \mathbb{R}$. The solution is a generalized soft shrinkage of x explained in the appendix.

Remark 3 (Computation of the strain ε within the primal-dual algorithm). *The primal-dual method uses the Lagrangian of (11), which contains the summand $\langle (\nabla u - a) - s, b \rangle$, with the dual variable b . Hence, the algorithm computes the desired strain tensor directly within the iteration process and no subsequent computation of the derivative of the optical flow is required.*

We updated the basic PDHGMP algorithm by a coarse-to-fine scheme as proposed, e.g., in [2, 8, 27, 28] to cope with large displacements. Moreover, we applied the common trick median filtering on every scale to improve the results, see also [27, 28]. For more information and the pseudo code for the coarse-to-fine scheme we refer to [15].

4 Numerical Examples

In this section, we present and analyze numerical results of our approaches.

First, we consider artificial data to demonstrate the behavior of different optical flow models and to underline why the TGV regularized model appears to be appropriate for the described practical tasks. Then, we deal with displacements in aluminum matrix composites (AMC) during tensile tests, where we focus on the detection of local damage and crack propagation. Finally, we demonstrate the flexibility of our method by showing results for different experimental settings and materials.

The algorithm is implemented in C++. Unless stated otherwise, we set

$$\lambda_1 := 0.2 \text{ and } \lambda_2 := 10 \quad (13)$$

for all real-world examples. The positivity constraint (10) on the strain is used for the real-world examples of tensile tests with AMCs. For the artificial examples and the compression and fatigue tests, we do not involve the constraints.

The data in Figure 9 was provided by K. Lichtenberg from the “Institute for Applied Materials (IAM)” at the Karlsruhe Institute of Technology (KIT).

4.1 Artificial Examples

To explain the differences between various regularization terms, we use the following simple example: a segment of 100×100 pixels of one exemplary micrograph of an aluminum composite is taken and the simulated displacement field in **Figure 2** consisting of the sum of a piecewise constant and a linear part is applied to warp this image. Then, the warped and the initial image are used as the input to reconstruct the simulated displacement field and its strain tensor via variational models with the same data term (8) and the following priors: besides the TGV prior, we used the

- i) H^1 regularizer, e.g., used in the Horn-Schunck model [19],

$$\lambda H^1(u) := \lambda \|\nabla u\|_2^2, \quad (H^1)$$

- ii) TV regularizer proposed in [23] and used for optical flow, e.g. in [8],

$$\lambda \text{TV}(u) := \lambda \|\nabla u\|_{2,1}, \quad (\text{TV})$$

- iii) TV_2 regularizer with second order differences

$$\lambda \text{TV}_2(u) := \lambda \|\nabla^2 u\|_{2,1}, \quad (\text{TV}_2)$$

- iv) TV - TV_2 regularizer, e.g. in [20],

$$\text{TV}_{1-2}(u) := \lambda_1 \|\nabla u\|_{2,1} + \lambda_2 \|\nabla^2 u\|_{2,1}, \quad (\text{TV} - \text{TV}_2)$$

- v) IC regularizer

$$\text{IC}(u) := \min_{u=v+w} \lambda_1 \|\nabla v\|_{2,1} + \lambda_2 \|\nabla^2 w\|_{2,1} + \lambda_3 \|w\|_2^2, \quad (\text{IC})$$

where we added a small quadratic term to ensure uniqueness of the decomposition. To obtain comparable results, we set λ_1, λ_2 as in the TGV model and $\lambda_3 := 5 \cdot 10^{-5}$.

The minimizers u_1 of the various models and the strain component $\varepsilon_{11} = \nabla_x u_1$ are shown in **Figures 3a** and **3b**, respectively. The parameters stated in the caption are optimized with respect to the best visual impression.

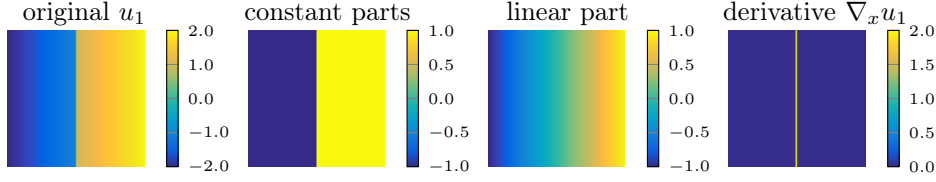


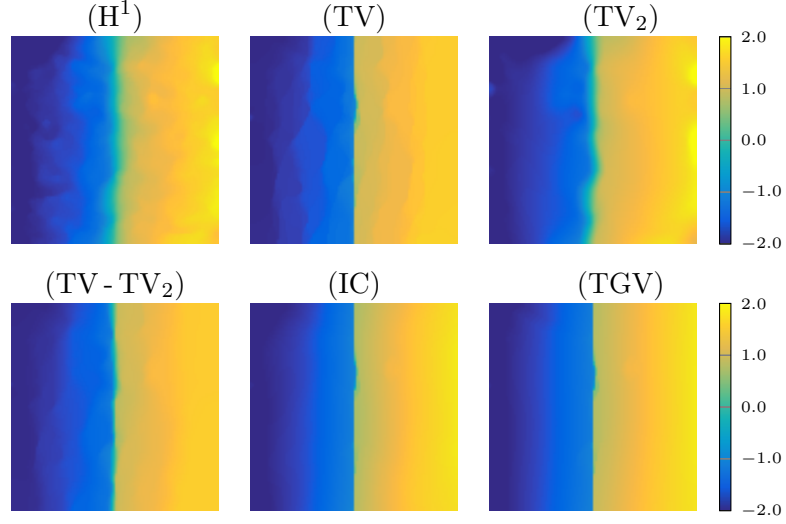
Figure 2: Original displacement u_1 in pixels, additively composed of a piecewise constant and a linear part and $\nabla_x u_1$.

The models with H^1 and TV_2 priors cannot find a sharp displacement field boundary, while the TV model introduces additional boundaries due to the so-called staircasing effect. The TV- TV_2 regularized model is better, but it is clearly worse than the IC and TGV methods. Clearly, for this example both methods IC and TGV give good results since u_1 is indeed additively composed of a non-smooth and a smooth component. The next example does not have this property.

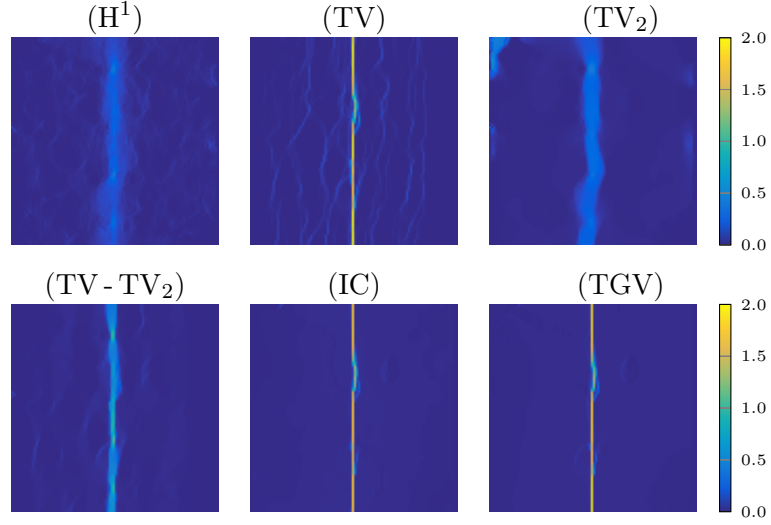
Our next artificial example in **Figure 4** shows a displacement field consisting of two parts. The lower part contains a jump whereas we have a purely linear transition in the upper part. In terms of a tensile test, this might be seen as a crack in the lower part and a purely elastic deformation in the upper part of the image. As the displacement field is a transition between the non-smooth upper part and the smooth lower one, it can not be split additively in an appropriate way, whereas it is actually possible to split the strain. Therefore, the TGV model clearly outperforms the IC model. The parameters for the TGV model are those in (13). For the IC model, we chose smaller parameters $\lambda_1 = 0.1$, $\lambda_2 = 1$ since otherwise the resulting displacement was too smooth.

4.2 Tensile Tests with AMC

Next, we deal with tensile tests of aluminum matrix composites (AMC). An AMC material is highly suitable for lightweight applications in aerospace, defense and automotive industry. Compared to monolithic materials, composite materials have advantageous properties such as higher ultimate tensile strength or a higher stiffness to density ratio. Here, we mainly focus on calculating local strains of silicon carbide particle reinforced AMCs from a sequence of scanning electron microscope (SEM) images acquired during tensile tests, where the specimen is pulled in x -direction and elongates with increasing force. Figure 1 illustrates the experimental setup and the resulting image sequence schematically. We are interested in the local deformation behavior of the composite material on a microscale. Therefore, it is necessary to perform SEM monitored tensile tests to study deformation and crack initiation due to the inhomogeneous microstructure. We will especially focus on ε_{11} , which describes the change in displacement u_1 for the x -direction. A

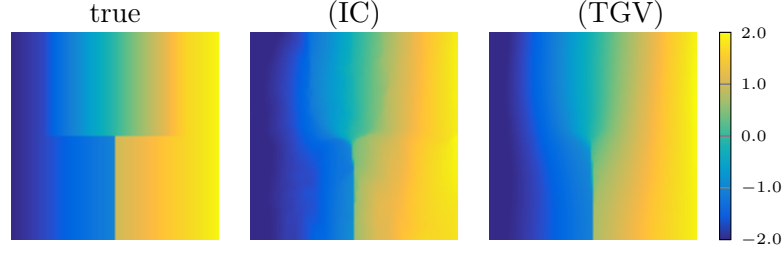


(a) Displacement u_1 in pixels using various regularization terms.

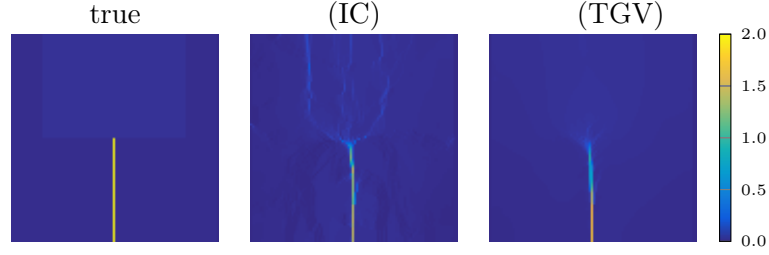


(b) Derivative $\nabla_x u_1$ using various regularization terms.

Figure 3: Results for the simulated example from **Figure 2** for various regularization terms. Parameters: $\lambda = 50$ for (H^1) , $\lambda = 0.1$ for (TV) , $\lambda = 0.1$ for (TV_2) , $\lambda_1 = 0.1$, $\lambda_2 = 0.02$ for $(TV - TV_2)$, $\lambda_1 = 0.1$, $\lambda_2 = 2$ for (IC) and $\lambda_1 = 0.1$, $\lambda_2 = 1$, $\lambda_3 = 0.5 \cdot 10^{-5}$ for (TGV) .



(a) Displacement u_1 in pixels using IC and TGV regularization.



(b) Derivative $\nabla_x u_1$ using IC and TGV regularization.

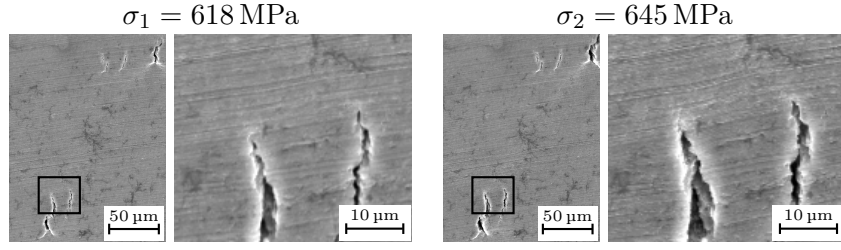
Figure 4: Results for a simulated example with a linear transition of the displacement field in the upper half and a jump in the lower half of the image.

positive value indicates tension and a negative one compression.

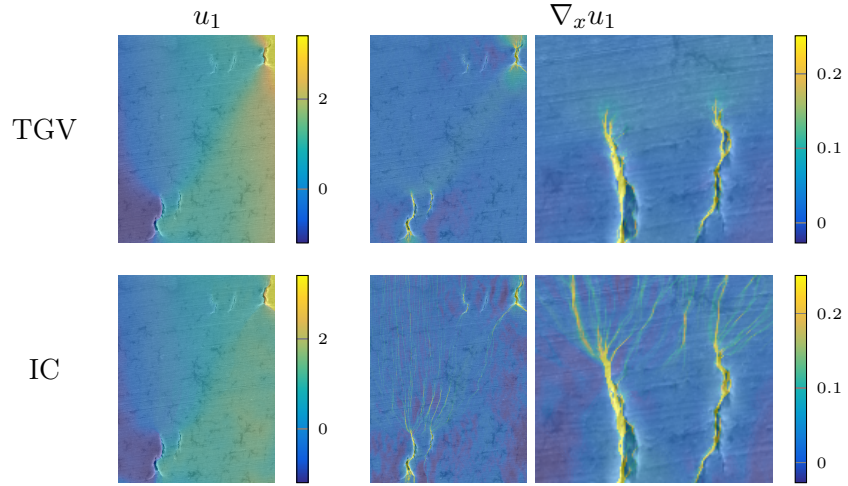
Unless stated otherwise, we use the image under no or low load as the reference image f_1 and compute the displacement between the reference image and images under higher load. Hence, the displacement and strain are given in the coordinates of the reference image and we overlay the results with the reference image.

The real-world example in **Figure 5** illustrates again the difference between the TGV and IC regularized models. In this example, the material has a few cracks in its initial state and they widen up, but the surrounding aluminum matrix deforms smoothly. Whereas the computed displacement u_1 looks roughly the same for both methods, the differences are visible in its derivative $\nabla_x u_1$. The TGV model only shows some structure where the cracks actually are, but the IC model leads to structures that pass through the whole image since it is, in analogy to the previous artificial example, impossible to split the displacement into two parts for this example. The TGV model outperforms the IC model in this setting. Nevertheless, for the cracks themselves, both methods lead to equally good results as the lower half of the enlarged region in Figure 5 shows. In summary, both methods show the main structures, but the IC model introduces wrong structures. Therefore, we focus on the TGV model in the rest of our examples.

In our next example, we are interested in the detection of different kind



(a) Microstructure images of the specimen under low and high load.



(b) Results of the TGV and IC models showing the displacement u_1 in μm ($1 \mu\text{m} = 4 \text{px}$) and the strain $\nabla_x u_1$.

Figure 5: Comparison of IC and TGV models for a real-world example where the cracks widen up but the surrounding aluminum matrix deforms smoothly.

of cracks. **Figure 6** shows other real-world data arising from a tensile test. Cracks correspond to peaks in $\nabla_x u_1$. In the enlarged regions, three different types of cracks are shown, namely

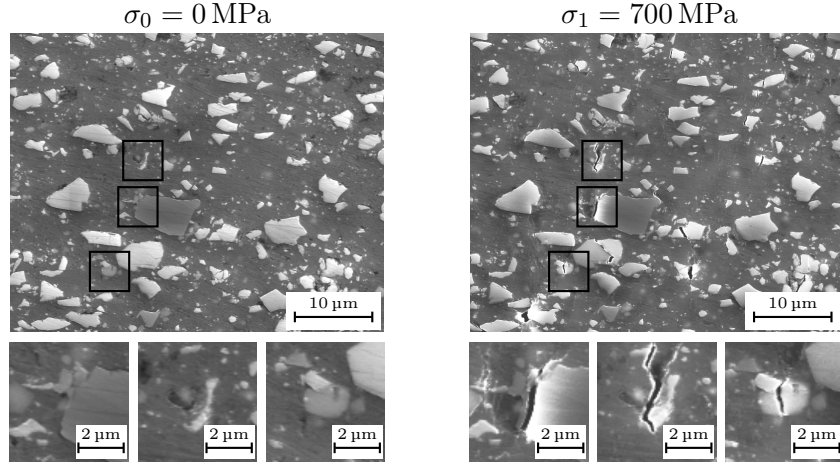
- i) a crack due to decohesion of a particle from the surrounding matrix,
- ii) a crack in the aluminum matrix, and
- iii) a crack inside a particle.

Next, we are interested in crack propagation. **Figure 7** shows the displacement u_1 and the strain $\varepsilon_{11} = \nabla_x u_1$ for certain regions under different load. It is remarkable that even under low load, when the cracks are not or hardly visible in the images, the strain in the corresponding regions is large. Thus, it is a sensitive and useful tool to study crack initiation mechanisms.

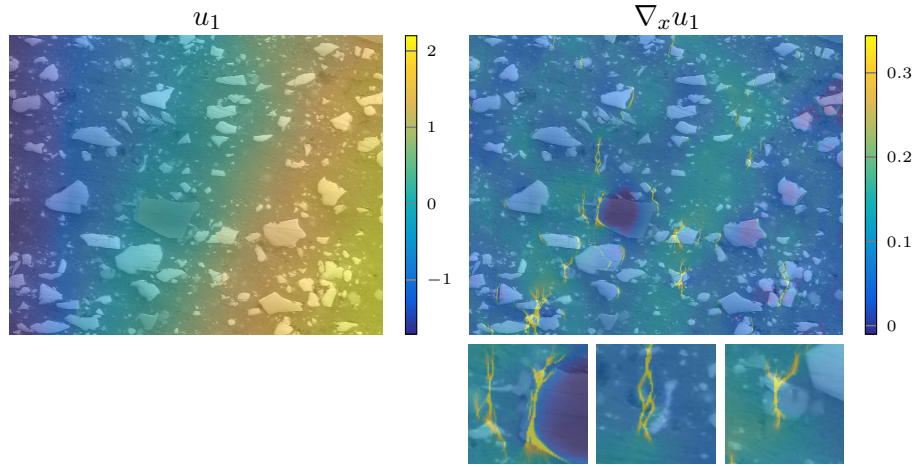
Comparison to Correlation Based Methods. Now, we draw our attention to a comparison of the proposed method to correlation based methods. In the following, we use NCorr [5] for a comparison since it is a freely available software package. Note that other state-of-the-art software packages for strain analysis such as Veddac [12] or VIC [14] are based on similar methods. In particular in [16], it is shown that NCorr produces equally good results as VIC. The underlying idea of correlation based methods is the comparison of windows around each pixel in certain search windows. Due to the extent of the window around the pixels, the local resolution of such methods is limited. **Figure 8** shows three examples where the proposed TGV regularized method is compared to NCorr. The first example in Figure 8 shows the same specimen as Figure 5. Although the cracks are relatively large, it is not possible to resolve them with NCorr and there occur some artifacts around them. Thus, the low resolution is especially a drawback in our applications since we are interested in the local behavior and in particular cracks. Besides the cracks, the smooth parts look very similar to the result using the proposed method. For the cracks, a_1 is a good result. A peak is visible at the crack tip, which is the position where the crack is expected to propagate. In contrast, the result of NCorr shows a peak everywhere around the crack.

The second and third example show more complicated deformations. In addition to $\nabla_x u_1$, we depict the smooth strain part a_1 , that is split off by the TGV regularizer. It is visible that the result of NCorr looks very similar to a_1 , in particular the same peaks and structures in a degree of $\pm \frac{\pi}{4}$ can be observed. But in addition to this smooth part, which resembles the strain in the classical meaning in materials science, our method is able to resolve also the local damage.

In summary, the proposed method is on the one hand able to extract the information that also commercial software extracts. This warrants that the model in general gives correct results from the viewpoint of materials

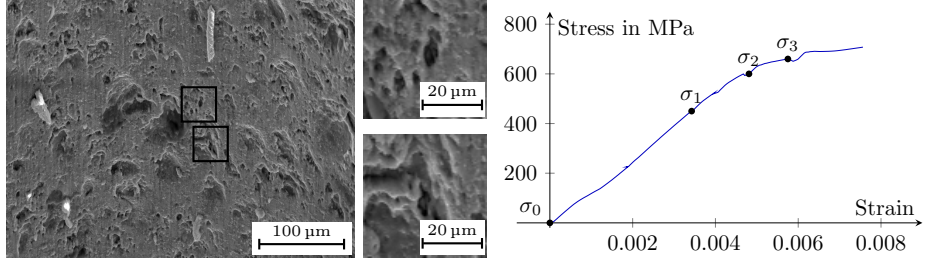


(a) Microstructure images of the specimen under low and high load.

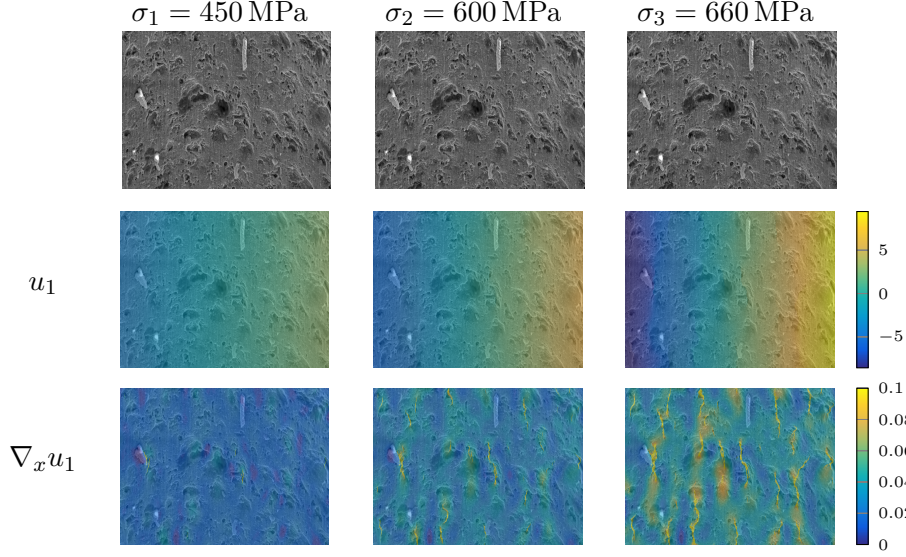


(b) Results of the TGV model showing the displacement u_1 in μm ($1 \mu\text{m} = 16 \text{ px}$) and the strain $\nabla_x u_1$.

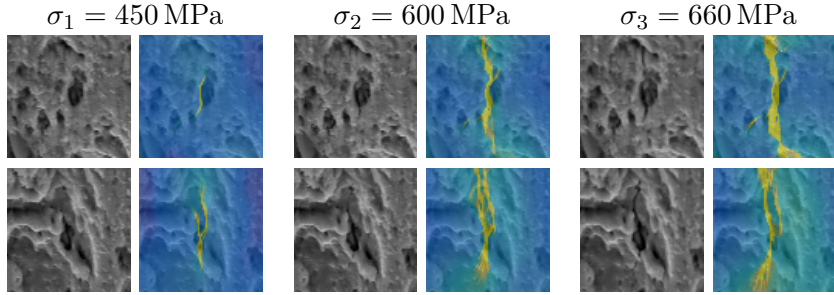
Figure 6: Detection of different kind of cracks by the TGV model.



(a) Microstructure images without load ($\sigma_0 = 0$ MPa) and stress-strain curve.



(b) Displacement u_1 in μm ($1 \mu\text{m} = 2 \text{px}$) and the strain $\nabla_x u_1$. The colorbar for the strain is cut off at 0.1 to make smaller values under low load visible.



(c) Two enlarged regions and the strain $\nabla_x u_1$ for increasing loads. The color map for the strain is cut off at 0.1 to make smaller values under low load visible.

Figure 7: Results on crack propagation by the TGV model.

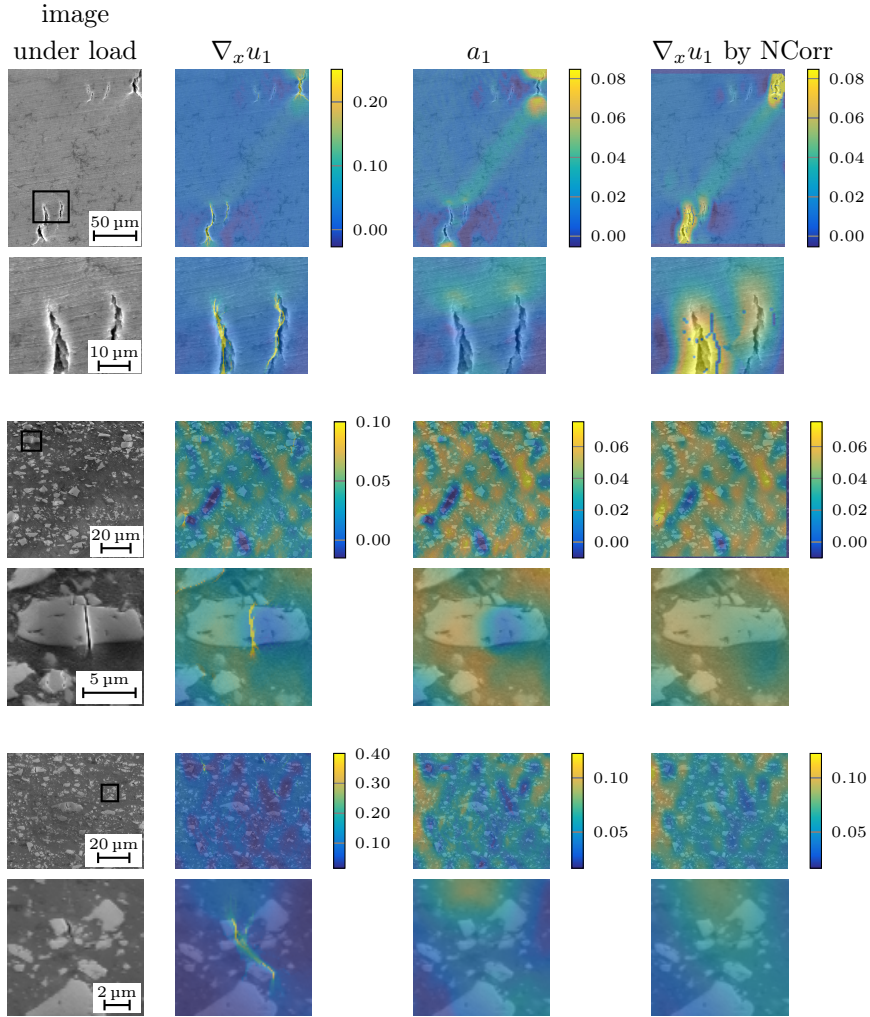


Figure 8: Comparison of the proposed model to the correlation based method NCorr for three different image pairs and enlarged regions.

science. On the other hand, it is possible to visualize the local behavior with a very high resolution where correlation-based methods fail.

4.3 Results for Other Materials and Experimental Settings

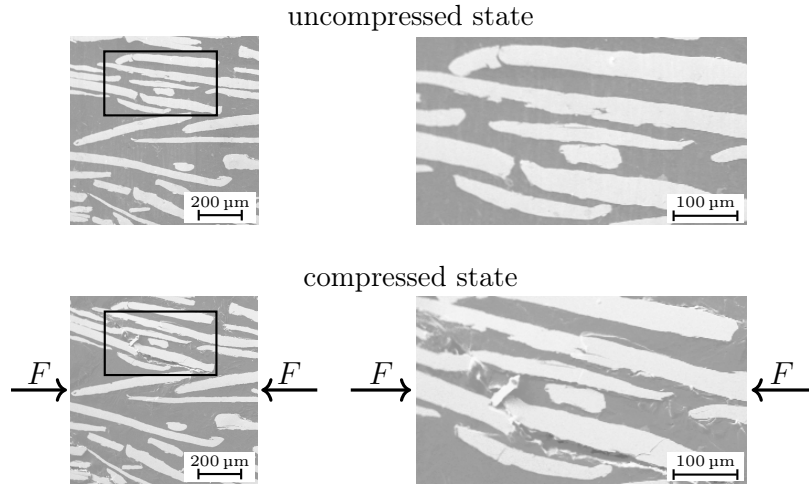
Finally, we leave the setting of tensile tests and show some results for other experimental settings and materials.

Figure 9 contains results for a compression test of a fiber reinforced aluminum matrix where load was applied in x -direction. Since the material is compressed in x -direction, cracks are expected to open up in y -direction. Hence, we depict also u_2 and $\nabla_y u_2$ since these are more suitable for this setting. Also in this case, the proposed method provides reasonable results and resolves cracks.

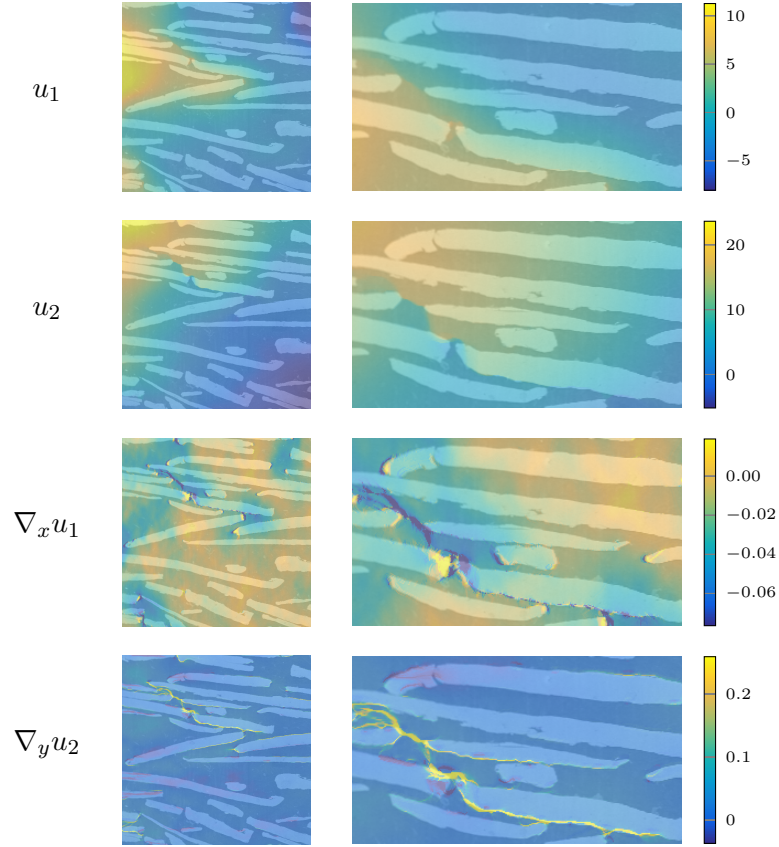
Figure 10 shows the results for a fatigue test. Here, we depict the images and results for one load cycle illustrated in Figure 10a. The first image shows the specimen in state “A” without load $\sigma_A = 0$ MPa, then load is applied, i.e., state “B” with $\sigma_B = 632$ MPa. For the third image, i.e. state “C”, the load is released again, i.e., $\sigma_C = 0$ MPa and then the specimen is compressed to state “D” with $\sigma_D = -630$ MPa. For the last image in state “E”, the load is released again, i.e., $\sigma_E = 0$ MPa. We use the image of state “A” as the reference image. The computed results are shown in Figure 10b. Similar to the previous examples of tensile tests, we see that the strain is positive almost everywhere for the image under load and we see exactly where cracks open up. For state “C”, which corresponds to the state after releasing the tension, the strain is mainly positive as well since only the elastic deformation reverses. For the image under compression, the displacement u_1 slightly decreases from left to right and the strain is mainly negative. In the last state “E” after completing the load cycle, the specimen is slightly more strained than in the initial state “A”. In particular, the crack in the particle opened up a bit. This is visible in the strain component $\nabla_x u_1$. Also the stress-strain curve in Figure 10a shows a positive strain for state “E”.

5 Conclusions

In this paper, we proposed a variational optical flow model for computing engineering strains on a microscale. Motivated by the setting of tensile tests, several first and a second order terms were evaluated for regularization. The method of our choice is a TGV regularized model with an optional constraint on the strain based on physical assumptions. The primal-dual method for finding a minimum of the corresponding energy function is especially suited since it directly computes the strain tensor within the iteration process. The results of the proposed model can be used for the detection of cracks and for an analysis of crack initiation and propagation. A comparison to

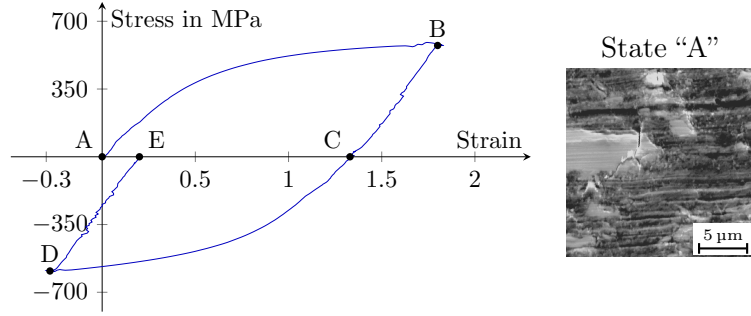


(a) Microstructure images of the uncompressed and compressed state.

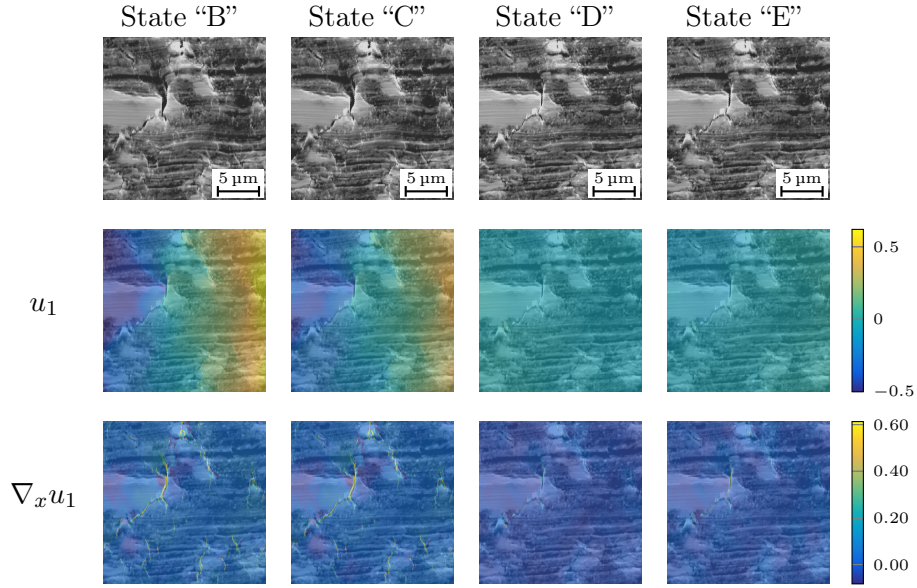


(b) Displacement u_1 , u_2 in μm ($10\mu\text{m} = 6\text{px}$) and the strain $\nabla_x u_1$, $\nabla_y u_2$.

Figure 9: Results for a compression test of a fiber reinforced aluminum matrix.



(a) Hysteresis curve of one cycle of a fatigue experiment and microstructure image of the initial state “A”.



(b) Results for the states shown in (a). Displacement u_1 in μm ($1 \mu\text{m} = 32 \text{px}$) and the strain $\nabla_x u_1$.

Figure 10: Results for different states of a fatigue test. An exemplary hysteresis curve is shown in (a), the results for the states “A”-“E” are shown in (b).

state-of-the-art software used for strain analysis showed that the proposed method clearly outperforms this software, in particular when analyzing the local strain. Further, it highlights microstructural damage as an additional benefit. We have shown that, besides tensile tests with AMCs, the method is also applicable for different materials as well as in other experiments such as compression and fatigue tests.

Acknowledgement

The authors thank K. Lichtenberg from the “Institute for Applied Materials (IAM)” at the Karlsruhe Institute of Technology (KIT) for providing the data in Figure 9. Funding by the German Research Foundation (DFG) within the Research Training Group 1932 “Stochastic Models for Innovations in the Engineering Sciences”, project area P3, is gratefully acknowledged.

A Soft and Coupled Shrinkage

The following two propositions state well-known facts (see e.g. [9]), which are required to compute the proximal maps in Algorithm 1.

Proposition 4. *Let $x \in \mathbb{R}$. Then,*

$$\hat{y} = \arg \min_{y \in \mathbb{R}} \left\{ \lambda |y| + \frac{1}{2} (y - x)^2 \right\}$$

is given by the soft shrinkage

$$\hat{y} = S_\lambda(x) := \begin{cases} 0 & \text{if } |x| \leq \lambda, \\ x(1 - \frac{\lambda}{|x|}) & \text{if } |x| > \lambda. \end{cases} \quad (14)$$

Proposition 5. *Let $x \in \mathbb{R}^d$. Then,*

$$\hat{y} = \arg \min_{y \in \mathbb{R}^d} \left\{ \lambda \|y\|_2 + \frac{1}{2} \|y - x\|_2^2 \right\}$$

is given by the grouped or coupled shrinkage

$$\hat{y} = \mathbf{S}_\lambda(x) := \begin{cases} 0 & \text{if } \|x\|_2 \leq \lambda, \\ x(1 - \frac{\lambda}{\|x\|_2}) & \text{if } \|x\|_2 > \lambda. \end{cases}$$

Computation of (12). Finally, we compute for given $x \in \mathbb{R}^2$ the value

$$\hat{y} = \arg \min_{y \in \mathbb{R}^2} \left\{ |\alpha y_1 + \beta y_2 + \gamma| + \frac{1}{2} \|x - y\|_2^2 \right\},$$

where $\alpha, \beta, \gamma \in \mathbb{R}$. We need to distinguish the following cases:

i) $\alpha = \beta = 0$: This gives obviously $\hat{y} = x$.

ii) $\alpha = 0, \beta \neq 0$: Here, we get $\hat{y}_1 = x_1$ and

$$\begin{aligned}\hat{y}_2 &= \arg \min_{y_2 \in \mathbb{R}} \left\{ |\beta y_2 + \gamma| + \frac{1}{2}(x_2 - y_2)^2 \right\} \\ &= \arg \min_{y_2 \in \mathbb{R}} \left\{ |y_2 + \frac{\gamma}{\beta}| + \frac{1}{2|\beta|}(x_2 - y_2)^2 \right\} \\ &= S_{|\beta|} \left(x_2 + \frac{\gamma}{\beta} \right) - \frac{\gamma}{\beta}\end{aligned}$$

with the soft shrinkage operator $S_{|\beta|}$

For $\alpha \neq 0, \beta = 0$, we get analogously

$$(\hat{y}_1, \hat{y}_2) = \left(S_{|\alpha|} \left(x_1 + \frac{\gamma}{\alpha} \right) - \frac{\gamma}{\alpha}, x_2 \right).$$

iii) $\alpha, \beta \neq 0$: By substitution, we get the following equivalent minimization problem:

$$(\hat{z}_1, \hat{z}_2) = \arg \min_{z \in \mathbb{R}^2} \left\{ |z_1 + z_2| + \frac{1}{2\lambda_1}(z_1 - \tilde{x}_1)^2 + \frac{1}{2\lambda_2}(z_2 - \tilde{x}_2)^2 \right\}$$

with

$$\begin{aligned}z_1 &:= \alpha y_1, & \tilde{x}_1 &:= \alpha x_1, & \lambda_1 &:= \alpha^2 > 0, \\ z_2 &:= \beta y_2 + \gamma, & \tilde{x}_2 &:= \beta x_2 + \gamma, & \lambda_2 &:= \beta^2 > 0.\end{aligned}$$

The following proposition provides a solution to the minimization problem.

Proposition 6. *Let $(x_1, x_2)^T \in \mathbb{R}^2$. Then, the unique minimizer of*

$$F(z_1, z_2) := |z_1 + z_2| + \frac{1}{2\lambda_1}(z_1 - \tilde{x}_1)^2 + \frac{1}{2\lambda_2}(z_2 - \tilde{x}_2)^2$$

is given by

$$(\hat{z}_1, \hat{z}_2) = \begin{cases} (\tilde{x}_1 - \lambda_1, \tilde{x}_2 - \lambda_2) & \text{if } \tilde{x}_1 + \tilde{x}_2 > \lambda_1 + \lambda_2, \\ (\tilde{x}_1 + \lambda_1, \tilde{x}_2 + \lambda_2) & \text{if } \tilde{x}_1 + \tilde{x}_2 < -(\lambda_1 + \lambda_2), \\ \left(\frac{\tilde{x}_1 \lambda_2 - \lambda_1 \tilde{x}_2}{\lambda_1 + \lambda_2}, \frac{\tilde{x}_2 \lambda_1 - \lambda_2 \tilde{x}_1}{\lambda_1 + \lambda_2} \right) & \text{otherwise.} \end{cases}$$

Proof. Since F is not differentiable at $z_1 = -z_2$, we distinguish whether $\hat{z}_1 + \hat{z}_2 = 0$ or not.

- i) $\hat{z}_1 + \hat{z}_2 \neq 0$: First, we assume that $\hat{z}_1 + \hat{z}_2 > 0$. Since F is differentiable around \hat{z} , we can compute the gradient and set it to zero, i.e.,

$$0 = \begin{pmatrix} 1 \\ 1 \end{pmatrix} + \begin{pmatrix} \frac{1}{\lambda_1}(\hat{z}_1 - \tilde{x}_1) \\ \frac{1}{\lambda_2}(\hat{z}_2 - \tilde{x}_2) \end{pmatrix}.$$

Hence, we obtain

$$(\hat{z}_1, \hat{z}_2) = (\tilde{x}_1 - \lambda_1, \tilde{x}_2 - \lambda_2)$$

and $\hat{z}_1 + \hat{z}_2 > 0$ if and only if $\tilde{x}_1 + \tilde{x}_2 > \lambda_1 + \lambda_2$. Analogously, one can show $(\hat{z}_1, \hat{z}_2) = (\tilde{x}_1 + \lambda_1, \tilde{x}_2 + \lambda_2)$ for $\tilde{x}_1 + \tilde{x}_2 < -(\lambda_1 + \lambda_2)$.

- ii) $\hat{z}_1 + \hat{z}_2 = 0$: Then $\hat{z}_1 = -\hat{z}_2$ and we obtain

$$\hat{z}_1 = \arg \min_{z_1 \in \mathbb{R}} \left\{ \frac{1}{2\lambda_1}(z_1 - \tilde{x}_1)^2 + \frac{1}{2\lambda_2}(z_1 + \tilde{x}_2)^2 \right\}.$$

Setting the derivative to zero leads to

$$0 = \frac{1}{\lambda_1}(\hat{z}_1 - \tilde{x}_1) + \frac{1}{\lambda_2}(\hat{z}_1 + \tilde{x}_2).$$

Thus, the solution is given by

$$\hat{z}_1 = \frac{\tilde{x}_1\lambda_2 - \lambda_1\tilde{x}_2}{\lambda_1 + \lambda_2} \quad \text{and} \quad \hat{z}_2 = \frac{\tilde{x}_2\lambda_1 - \lambda_2\tilde{x}_1}{\lambda_1 + \lambda_2}.$$

□

Remark 7. The soft shrinkage (14) is obtained in the special case $\lambda_1 = \lambda_2$ and $\tilde{x}_1 = \tilde{x}_2$.

References

- [1] L. Alvarez, C. Castaño, M. García, K. Krissian, L. Mazorra, A. Salgado, and J. Sánchez. Variational second order flow estimation for PIV sequences. *Experiments in Fluids*, 44(2):291–304, 2008.
- [2] P. Anandan. A computational framework and an algorithm for the measurement of visual motion. *International Journal of Computer Vision*, 2(3):283–310, 1989.
- [3] F. Balle, D. Eifler, J. H. Fitschen, S. Schuff, and G. Steidl. Computation and visualization of local deformation for multiphase metallic materials by infimal convolution of TV-type functionals. In *International Conference on Scale Space and Variational Methods in Computer Vision*, pages 385–396. Springer, 2015.

- [4] F. Becker, S. Petra, and C. Schnörr. Optical flow. In O. Scherzer, editor, *Handbook of Mathematical Methods in Imaging*, pages 1945–2004. Springer, New York, 2015.
- [5] J. Blaber, B. Adair, and A. Antoniou. Ncorr: Open-source 2D digital image correlation Matlab software. *Experimental Mechanics*, 55(6):1105–1122, 2015.
- [6] J. Braux-Zin, R. Dupont, and A. Bartoli. A general dense image matching framework combining direct and feature-based costs. In *IEEE International Conference on Computer Vision*, 2013.
- [7] K. Bredies, K. Kunisch, and T. Pock. Total generalized variation. *SIAM Journal on Imaging Sciences*, 3(3):492–526, 2010.
- [8] T. Brox, A. Bruhn, N. Papenberger, and J. Weickert. High accuracy optical flow estimation based on a theory for warping. In *European Conference on Computer Vision*, pages 25–36. Springer, 2004.
- [9] M. Burger, A. Sawatzky, and G. Steidl. First order algorithms in variational image processing. In R. Glowinski, S. Osher, and W. Yin, editors, *Operator Splittings and Alternating Direction Methods*. Springer, 2016.
- [10] A. Chambolle and P.-L. Lions. Image recovery via total variation minimization and related problems. *Numerische Mathematik*, 76(2):167–188, 1997.
- [11] A. Chambolle and T. Pock. A first-order primal-dual algorithm for convex problems with applications to imaging. *Journal of Mathematical Imaging and Vision*, 40(1):120–145, 2011.
- [12] Chemnitzer Werkstoffmechanik GmbH. VEDDAC – digital image correlation software. <http://www.cwm-chemnitz.de/>, 2017.
- [13] T. Corpetti, E. Memin, and P. Perez. Dense estimation of fluid flows. *IEEE Transactions on Pattern Analysis and Machine Intelligence*, 24(3):365–380, 2002.
- [14] Correlated Solutions Inc. VIC 2D – digital image correlation software. <http://correlatedsolutions.com/vic-2d/>, 2017.
- [15] J. H. Fitschen. *Variational Models in Image Processing with Applications in the Materials Sciences*. PhD thesis, University of Kaiserslautern, 2017.
- [16] R. Harilal and M. Ramji. Adaptation of open source 2D DIC software Ncorr for solid mechanics applications. In *International Symposium on Advanced Science and Technology in Experimental Mechanics*, 2014.

- [17] A. Hewer, J. Weickert, H. Seibert, T. Scheffer, and S. Diebels. Lagrangian strain tensor computation with higher order variational models. In *British Machine Vision Conference*. BMVA Press, 2013.
- [18] M. Holler and K. Kunisch. On infimal convolution of TV-type functionals and applications to video and image reconstruction. *SIAM Journal on Imaging Sciences*, 7(4):2258–2300, 2014.
- [19] B. K. Horn and B. G. Schunck. Determining optical flow. *Artificial Intelligence*, 17(1-3):185–203, 1981.
- [20] K. Papafitsoros and C. B. Schönlieb. A combined first and second order variational approach for image reconstruction. *Journal of Mathematical Imaging and Vision*, 2(48):308–338, 2014.
- [21] T. Pock, A. Chambolle, D. Cremers, and H. Bischof. A convex relaxation approach for computing minimal partitions. In *IEEE Conference on Computer Vision and Pattern Recognition*, pages 810–817, 2009.
- [22] R. Ranftl, K. Bredies, and T. Pock. Non-local total generalized variation for optical flow estimation. In *European Conference on Computer Vision*, pages 439–454. Springer, 2014.
- [23] L. Rudin, S. Osher, and E. Fatemi. Nonlinear total variation based noise removal algorithms. *Physica D: Nonlinear Phenomena*, 60(1):259–268, 1992.
- [24] S. Scherer, P. Werth, and A. Pinz. The discriminatory power of ordinal measures - towards a new coefficient. In *IEEE Conference on Computer Vision and Pattern Recognition*, pages 76–81, 1999.
- [25] S. Setzer and G. Steidl. Variational methods with higher order derivatives in image processing. In *Approximation XII: San Antonio 2007*, pages 360–385, 2008.
- [26] S. Setzer, G. Steidl, and T. Teuber. Infimal convolution regularizations with discrete ℓ_1 -type functionals. *Communications in Mathematical Sciences*, 9(3):797–827, 2011.
- [27] D. Sun, S. Roth, and M. J. Black. Secrets of optical flow estimation and their principles. In *IEEE Conference on Computer Vision and Pattern Recognition*, pages 2432–2439, 2010.
- [28] D. Sun, S. Roth, and M. J. Black. A quantitative analysis of current practices in optical flow estimation and the principles behind them. *International Journal of Computer Vision*, 106(2):115–137, 2014.

- [29] A. Tatschl and O. Kolednik. A new tool for the experimental characterization of micro-plasticity. *Materials Science and Engineering: A*, 339(1–2):265 – 280, 2003.
- [30] W. Trobin, T. Pock, D. Cremers, and H. Bischof. An unbiased second-order prior for high-accuracy motion estimation. In *DAGM Pattern Recognition Symposium*, pages 396–405. Springer, 2008.
- [31] C. Vogel, S. Roth, and K. Schindler. An evaluation of data costs for optical flow. In *German Conference on Pattern Recognition*, pages 343–353. Springer, 2013.
- [32] P. Werth and S. Scherer. A novel bidirectional framework for control and refinement of area based correlation techniques. In *IEEE International Conference on Pattern Recognition*, volume 3, pages 730–733, 2000.
- [33] J. Yuan, C. Schnörr, and E. Mémin. Discrete orthogonal decomposition and variational fluid flow estimation. *Journal of Mathematical Imaging and Vision*, 28:67–80, 2007.
- [34] J. Yuan, C. Schnörr, and G. Steidl. Simultaneous higher order optical flow estimation and decomposition. *SIAM Journal on Scientific Computing*, 29(6):2283–2304, 2007.